Electronic Supplementary Material (ESI) for Physical Chemistry Chemical Physics.

Supplementary Materials for Collision-induced torque mediates transition of chiral dynamic patterns formed by active particles

Tetsuya Hiraiwa[#a]
Mechanobiology Institute, National University of Singapore, Singapore 117411, Singapore and Universal Biology Institute, The University of Tokyo, Hongo, Tokyo 113-0033, Japan.

Ryo Akiyama[#]
Department of Chemistry, Kyushu University, Fukuoka 819-0395, Japan

Daisuke Inoue
Faculty of Design, Kyushu University, Fukuoka 815-0032, Japan

Arif Md. Rashedul Kabir and Akira Kakugo
Faculty of Science, Hokkaido University, Sapporo 060-0810, Japan

The content of the Supplementary Material is as follows:

- Supplementary texts
- Supplementary Figure 1 : Supplementary figure on the nature of the transition between homogeneous orientation and flocking states
- Supplementary Figure 2 : Supplementary figure on numerical simulations for dynamics of three particles in a regular square with periodic boundaries
- Supplementary Figure 3 : Supplementary figure on emerging dynamic patterns for the case with isotropic friction

[a] Electronic address : mbithi@nus.edu.sg

DETAILS OF THE THEORETICAL MODEL

We consider N particles in a square box with periodic boundaries in two dimensions, and assume that each particle is a self-propelled particle (SPP) with an intrinsic polarity along which the domain tries to move [1]. The location and intrinsic polarity of the j-th particle are described by $\boldsymbol{x}_j = (x_j; y_j)$ and $\boldsymbol{q}_j$, respectively ($j = 1; 2; \cdots; N$). We assume that the velocity $\boldsymbol{v}_j$, which determines the $\boldsymbol{x}_j$'s time evolution as

$$\frac{d\boldsymbol{x}_j}{dt} = \boldsymbol{v}_j \ ; \tag{S1}$$

and the polarity $\boldsymbol{q}_j$ of the j-th particle obeys

$$(\boldsymbol{q}_j)\boldsymbol{v}_j = v_0\boldsymbol{q}_j + \boldsymbol{J}^{\mathrm{VE}}{}_j \tag{S2}$$

and

$$\frac{d\boldsymbol{q}_j}{dt} = \boldsymbol{J}^{\mathrm{AL}}{}_j + \boldsymbol{\xi}_j + \boldsymbol{\omega}^{\mathrm{ST}} + \quad {}^{\mathrm{CT}}{}_j \tag{S3}$$

under the constraint $|\boldsymbol{q}_j| = 1$, respectively, for every j. Equation (S2) assumes the over-damped dynamics, and each particle moves with a constant velocity v_0 in the absence of volume exclusion interactions. Equation (S2) also assumes that each particle hardly moves along the direction perpendicular to the direction of $\boldsymbol{q}_j$, which has been implemented by the (rescaled) anisotropic friction tensor $\quad(\boldsymbol{q}_j) = \boldsymbol{q}_j \otimes \boldsymbol{q}_j + R^{-1}(\boldsymbol{I} - \boldsymbol{q}_j \otimes \boldsymbol{q}_j)$ with the ratio $R = {}_{\parallel}= {}_{\perp}$ of friction coefficients in parallel ${}_{\parallel}$ and perpendicular directions ${}_{\perp}$. Here, $\otimes$ is the tensor product, and $\boldsymbol{I}$ is the identity matrix. (The reason we introduced such anisotropy in friction is as follows: Ref. [1] observed that, when the gliding microtubule collides another microtubule from its side, the colliding microtubule either stops moving or gets over the other. In other words, phenomenologically, the microtubule collided from its side does not move into the direction perpendicular to its polarity. Since this work is motivated by the observations in microtubule gliding assay, as we detailed in Introduction of the main text, we reflected this fact phenomenologically by using the anisotropic mobility, or inverse friction, and below setting the friction perpendicular to the particle's intrinsic polarity to be much higher than the parallel counterpart, with which the particle hardly moves to the perpendicular direction indeed. However, it is to be noted that this anisotropic mobility is not essential in our main result.) The term $\boldsymbol{\xi}^q{}_j(t)$ represents the noise, for which, for simplicity, we assume a white Gaussian noise with $\langle \boldsymbol{\xi}^q{}_j \rangle = 0$ and

$$\langle \ {}^{q}_{i;k}(t) \ {}^{q}_{j;l}(t')\rangle = 2D \ {}_{ij} \ {}_{kl} \ (t - t') \ ; \tag{S4}$$

where the subscripts k and l specify the directions, $k; l = x; y$, with the statistical average $\langle\cdot\rangle$. The coefficient D indicates the noise strength. The particle-particle interactions are given by $\boldsymbol{J}^{\mathrm{VE}}{}_j$ and $\boldsymbol{J}^{\mathrm{AL}}{}_j$, which represent the volume exclusion and bidirectional alignment interaction with the interaction ranges r, respectively. The volume exclusion is given by

$$\boldsymbol{J}^{\mathrm{VE}}{}_j = \sum_{j'(n:j)} \frac{r}{|\Delta\boldsymbol{x}_{j;j'}|} - 1 \quad \frac{\Delta\boldsymbol{x}_{j;j'}}{|\Delta\boldsymbol{x}_{j;j'}|} \ : \tag{S5}$$

The summation $\sum_{j'(n:j)}$ runs for all the neighbors j' of j-th particles, defined by $|\Delta\boldsymbol{x}_{j;j'}| < r$ with $\Delta\boldsymbol{x}_{j;j'} = \boldsymbol{x}_j - \boldsymbol{x}_{j'}$. Here, we have assumed not rigorous but soft volume exclusion, and the softness is controlled by the factor $\quad$. Bidirectional alignment interaction is given by [1]

$$\boldsymbol{J}^{\mathrm{AL}}{}_j = 2 \ {}_{\mathrm{AL}} \sum_{j'(n:j)} (\boldsymbol{q}_j \cdot \boldsymbol{q}_{j'})\,\boldsymbol{q}_{j'} \ : \tag{S6}$$

The coefficient ${}_{\mathrm{AL}}$ indicates the strength of alignment. We can scrutinize the meaning of this term by rewriting it in the potential form;

$$\boldsymbol{J}^{\mathrm{AL}}{}_j = -\frac{@V(\{\boldsymbol{q}_i\})}{@\boldsymbol{q}_j} \tag{S7}$$

with

$$V(\{\boldsymbol{q}_i\} = - \ {}_{\mathrm{AL}} \sum_{j;j'\in n:p:} |\boldsymbol{q}_j \cdot \boldsymbol{q}_{j'}|^2 = - \ {}_{\mathrm{AL}} \sum_{j;j'\in n:p:} \cos^2(\ {}_j - \ {}_{j'}) \tag{S8}$$

The summation $\sum_{j;j'\in n:p:}$ runs for all the neighboring j-th and j'-th particle pairs, defined again by $|\Delta\boldsymbol{x}_{j;j'}| < r$. As Eqs. (S7) and (S8) indicate, this interaction term align the polarities of neighboring pair of particles in the bidirectional way, *i.e.* toward either $_j - _{j'} = 0$ or $_j - _{j'} =$. In this study, we naively assume given constants $_{\mathrm{AL}}$ and for the interaction, but there are other possible choices. For example, in some literature on collective motion of SPPs, the interaction is defined in the way that its strength depends on the SPP speed [2]. This may be the point which one has to be careful when investigating the phase diagram over *e.g.* v_0. In this paper, we focus on only the torque strengths, mentioned below, so that this choice may not affect the conclusion.

The last two terms of Eq. (S3) are the key terms of this study, which give rise to chirality. As mentioned in Introduction of the main text, in this article, we assume that chirality affects the system's dynamics through the two different ways: one is the self-propelled torque (ST) $\boldsymbol{\omega}^{\mathrm{ST}} \equiv \omega^{\mathrm{ST}}\boldsymbol{q}_j^{\perp}$, and the other is the collision-induced torque (CT) $^{\mathrm{CT}}{}_j \equiv \Omega_j^{\mathrm{CT}}\boldsymbol{q}_j^{\perp}$. Here, $\boldsymbol{q}_j^{\perp}$ is one of the unit vectors perpendicular to the polarity, given by $\boldsymbol{q}_j^{\perp} \equiv (-\sin\ _j; \cos\ _j)$. The constant ω^{ST} is the strength of ST. On the other hand, Ω_j^{CT} is given by $\Omega_j^{\mathrm{CT}} = \omega^{CT} m_j$ with the number m_j of particles within the range r from the focused particle (j), and the constant ω^{CT} controls the strength of CT. (See Fig. 1 in the main text for the schematics.) It is worth noted that, in two dimensions, there are two unit vectors perpendicular to a certain reference vector, corresponding to left or right. The above definition of $\boldsymbol{q}_j^{\perp}$ selected out one of them. Thus, the existence of $\boldsymbol{q}_j^{\perp}$ in the definitions of $\boldsymbol{\omega}^{\mathrm{ST}}$ and $^{\mathrm{CT}}$ is expressing the origin of chirality.

Equation (S3) can be rewritten as the time evolution of the angles $_j$ of the polarity directions, using $\boldsymbol{q}_j = (\cos\ _j; \sin\ _j)$. For this purpose, we may take the inner products of $\boldsymbol{q}_j^{\perp}$ and the both sides of Eq. (S3). As a result, Eq. (2) of the main text is obtained, with $_j \equiv \boldsymbol{\xi}_j \cdot \boldsymbol{q}_j^{\perp}$. The new noise term $_j(t)$ represents the angular noise, and since $_j = -\ ^q_{x;j} \sin\ _j + \ ^q_{y;j} \cos\ _j$, it is again a Gaussian white noise with $\langle\ _j\rangle = 0$ and

$$\langle\ \ (t)\ \ _{\prime}(t')\rangle = 2D\ \ _{;\ \prime}\ (t-t'): \tag{S9}$$

Note that D^{-1} now characterizes the persistence time of polarity direction, or characteristic time of angular fluctuation.

Equation (S2) and Eq. (2) of the main text, *i.e.*, the angular description of Eq. (S3), can be rewritten by the dimensionless forms as

$$\frac{d\tilde{\boldsymbol{x}}_j}{d\tilde{t}} = \boldsymbol{q} + \tilde{\ } \sum_{j'\ (n:j)} \frac{\tilde{\Delta\boldsymbol{x}}_{j;j'}}{|\tilde{\Delta\boldsymbol{x}}_{j;j'}|^2} \tag{S10}$$

and

$$\frac{d\ _j}{d\tilde{t}} = 2\tilde{\ }_{\mathrm{AL}} \sum_{j'(n:j)} (\boldsymbol{q}_j \cdot \boldsymbol{q}_{j'})\,(\boldsymbol{q}_j^{\perp} \cdot \boldsymbol{q}_{j'}) + \tilde{\ }_j + \omega^{\tilde{\mathrm{ST}}} + \Omega^{\tilde{\mathrm{CT}}}{}_j\ ; \tag{S11}$$

respectively, where $\tilde{\boldsymbol{x}}_j = \boldsymbol{x}_j/X$, $\tilde{t} = t/T$, $\tilde{\Delta\boldsymbol{x}}_{j;j'} = \Delta\boldsymbol{x}_{j;j'}/X$, $\tilde{\ } = \ T/X$, $\tilde{\ }_{\mathrm{AL}} = \ _{\mathrm{AL}}T$, $\omega^{\tilde{\mathrm{ST}}} = \omega^{\mathrm{ST}}T$ and $\Omega^{\tilde{\mathrm{CT}}}{}_j = \Omega^{\mathrm{CT}}{}_j T$, with characteristic length $X \equiv r$ and time $T \equiv r/v_0$. The noise term is also rescaled into the new notation $\tilde{\ }_j(t)$, which is a Gaussian white noise satisfying $\langle\tilde{\ }_j\rangle = 0$ and

$$\langle\tilde{\ }\ (t)\,\tilde{\ }_{\prime}(t')\rangle = 2\tilde{D}\ \ _{;\ \prime}\ (\tilde{t}-\tilde{t}'): \tag{S12}$$

with $\tilde{D} = DT$. In the main text, we applied the same nondimensionalization by putting $r = 1$ and $v_0 = 1$. The propulsion strength is often quantified by using Péclet number [3, 4]. The Péclet number, or specifically the rotational Péclet number [4], is defined by $\mathrm{Pe} \equiv v_0\ _p/r$, with the migration persistence time $_p$ [3]. Pe is given by the inverse of the dimensionless noise, $\mathrm{Pe} = \tilde{D}^{-1}$, because $_p = D^{-1}$ in our case. The parameter values which we used in our simulations here correspond to $\mathrm{Pe} = 100$.

A FEW NOTES REGARDING DENSITY IN FLOCKS

In the case that ST and CT are the same directions with each other (filled circles) in Fig. S1(b), the local density in mono-polar flocks is between 0:4 to 1:5 with the median of 1:0. When the density is 1:0, the packing is almost the closest. The density increases as the absolute value of the average angular velocity increases. This result suggests that the collisions generate the effective attraction and mono-polar flocks are maintained by the collisions.

The density increases as the absolute value of the mean rotation speed increases. The collision becomes more frequent and stronger as the torque becomes greater. We can regard that the effective attraction between the particles

is strong under such conditions. In the case that ST and CT are the opposite directions with each other (filled diamonds in Fig. S1(b)), this feature is remarkable. Therefore, we find the density 2.5 or more. The large value suggests, the particles overlay each other due to the strong collision. Here, the red diamonds for the high-density flocks belong to the island region of monopolar flocks in Fig. 3(b) and (d) in the main text because the red diamonds mean $!^{ST} > 1.5 \times 10^{-2}$. The strong collisions in the cluster caused by the CW-ST and the CCW-CT are confirmed in Fig. S1(b). These high-density flocks are clearly distinguished from the low-density homogeneous phase.

THREE-PARTICLE SIMULATION

Figure S2 provides additional results of numerical simulations for dynamics of three particles in a regular square with periodic boundaries. (The system width is set to be $L = \sqrt{N\pi}$ with $N = 3$ and $= 0.02$.) In the simulations here, the initial locations and polarities of the three SPPs are set in a triangular and inwardly-pointing manner, respectively, which allows three SPPs to effectively collide, as shown in Fig. S2(a) top left; $t = 0$. Typical snapshots of the simulation results are shown in Fig. S2(a,b). Here, we have applied $!^{CT} = 0.1$, which is much larger than the maximum strength used in the main text, $!^{CT} = 0.004$. As shown in Fig. S2(a), the three SPPs show various pair/triplet dynamics including the bi-directional orientation, merging into a single mono-polar flock, and split of the flock. In the main text, we found that the collision-induced torque can induce the mono-polar flocking. Figure S2(b) indeed demonstrates the case when a two-particle cluster rotates, which broke the bidirectional orientation, and results in formation of the mono-polar flock of three SPPs.

The results of such three-SPP simulations are quantified in Fig. S2(c,d) and Fig. 4(b) in the main text. Figure S2(c) plots rotation velocity V_R of intrinsic polarities during the particle-particle contact, averaged over all elements and time ($\langle\cdot\rangle$), against $!^{CT}$. It indeed increases linearly for increasing $!^{CT}$ on average. In Fig. S2(d), time evolution of the polar order R_p (red solid curve), nematic order R_n (green dotted curve) and contact numbers (blue broken curve) corresponding to the sample dynamics shown in Fig. S2(b), or Fig. 4(a) in the main text. The polar- and nematic-order parameters, R_p and R_n, are defined as

$$R_p(t) \equiv \sum_{i=1;2;3} \exp[i\ _i(t)] \ = \sum_{i=1;2;3} \boldsymbol{q}_i(t) \tag{S13}$$

and

$$R_n(t) \equiv \sum_{i=1;2;3} \exp[2i\ _i(t)] \ = \sum_{i=1;2;3} q_x^2(t) - q_y^2(t) + 2iq_x(t)q_y(t) \tag{S14}$$

respectively. The summation $\sum_{i=1;2;3}$ runs over three SPPs labelled by $i = 1; 2; 3$. We assume that two SPPs are in contact with each other if the distance of those two SPPs is smaller than the interaction range r, and contact number is defined as the number of such pairs in contact. Figure S2(d) also shows the mono-polar flock and bidirectional orientation regimes. Here, the mono-polar flock regime has been defined as the time window during which $R_p > R_{\mathrm{Th}}$ and the contact number is 2 or 3. The bidirectional orientation regime has been defined as the time window during which $R_n > R_{\mathrm{Th}}^2$, $R_p < R_{\mathrm{Th}}$ and the contact number is equal to or higher than 1. (We here set $R_{\mathrm{Th}} = 0.9$ again.) Although there is another short bidirectional orientation regime around $t = 100$ in Fig. S2(d), we skipped plotting it for better visibility. In Fig. 4(b) of the main text, we plotted the probability $P_{(t<128)}$ by which the three SPPs form the mono-polar flock at least a time by $t = 128$ for various $!^{CT}$ and $!^{ST}$. To define $P_{(t<128)}$ for each parameter set, we have counted the number of the samples which has mono-polar flock regimes at least a time until $t = 128$ and divided it by the total number of samples (128 samples).

[1] S. Tanida, K. Furuta, K. Nishikawa, T. Hiraiwa, H. Kojima, K. Oiwa and M. Sano, "Gliding filament system giving both orientational order and clusters in collective motion" Phys. Rev. E **101**, 032607 (2020).

[2] A. Baskaran and M C. Marchetti, "Enhanced Diffusion and Ordering of Self-Propelled Rods" Phys. Rev. Lett. **101**, 268101 (2008).

[3] G. S. Redner, M. F. Hagan, and A. Baskaran, "Structure and Dynamics of a Phase-Separating Active Colloidal Fluid" Phys. Rev. Lett. **110**, 055701 (2013).

[4] H.-S. Kuan, R. Blackwell, L. E. Hough, M. A. Glaser, and M. D. Betterton, "Hysteresis, reentrance, and glassy dynamics in systems of self-propelled rods" Phys. Rev. E **92**, 060501(R) (2015).

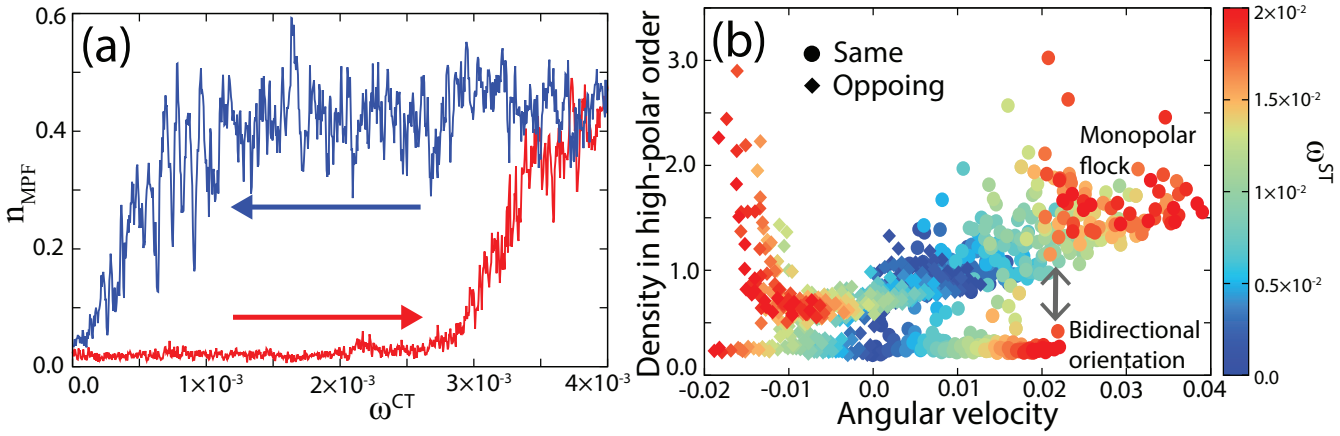

FIG. S1. First order transition-like nature of mono-polar flocking. (a) Hysteresis of SPP number fraction in mono-polar flocks, n_{MPF}. ω^{ST} is set to be 0.01, and ω^{CT} was swept from 0 to 0.004 (ascent; red curve) and, after that, *vice versa* (descent; blue curve). See the legend of Fig. 3(c,d) in the main text for the definition of n_{MPF}. (b) Local density in regions with high polar order, against the average angular velocity of each SPP. The color of each mark indicates the CT strength ω^{ST} whereas the shape indicates the direction of ST (circles and diamonds; the same as and opposite to CT, respectively). Multiple marks with the same color and shape correspond to various ω^{CT}.

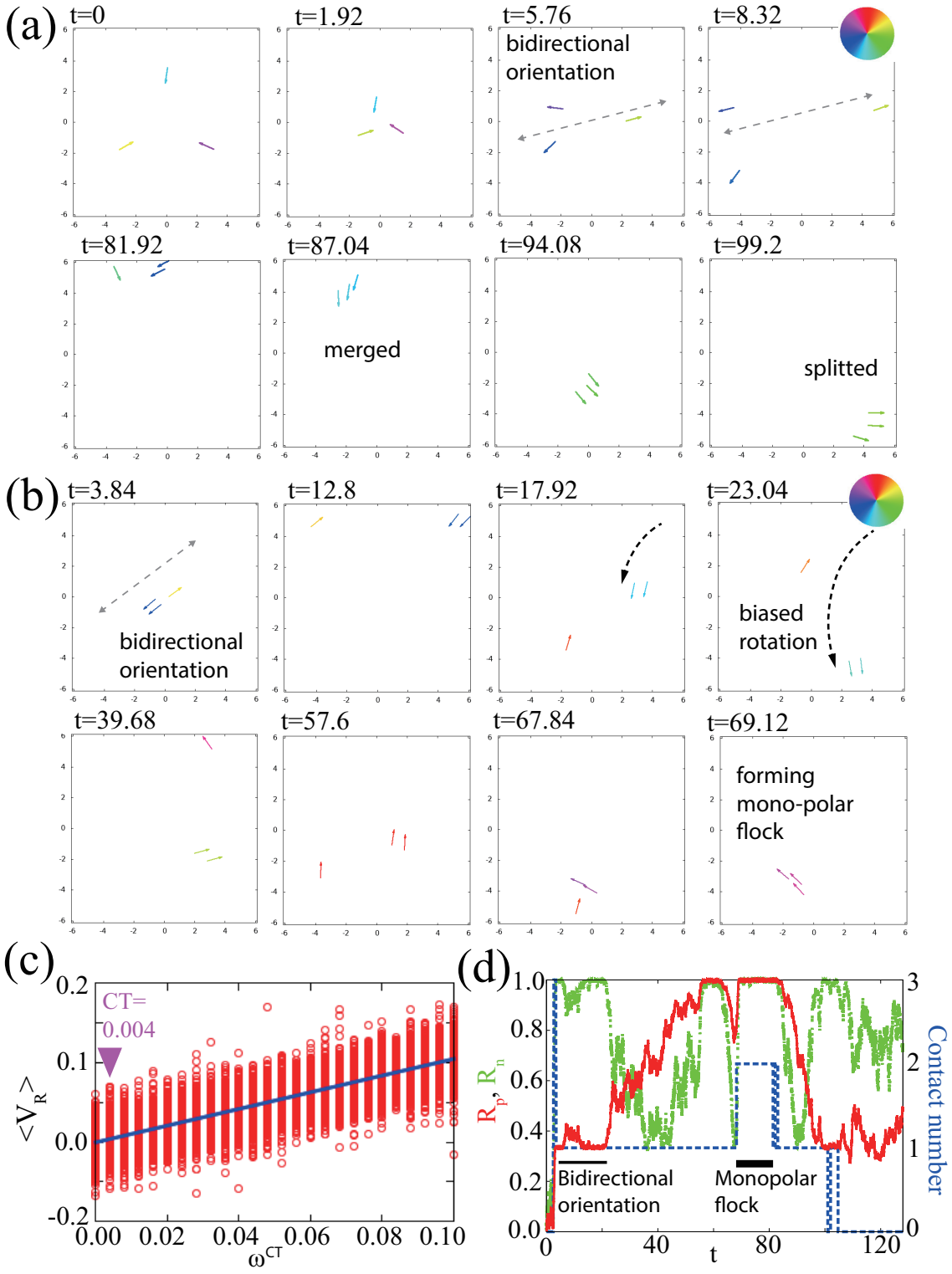

FIG. S2. Numerical simulations for dynamics of three particles in a regular square with periodic boundaries. (a) Snapshots for a single simulation. Each colored arrow represents the location and polarity direction of each particle, and the color indicates its polarity direction corresponding to the color wheel. $\omega^{\mathrm{CT}} = 0.1$, $\omega^{\mathrm{ST}} = 0.0$, and the other parameters are the same as in the main text. (b) Another sample with the same parameter values with (a). (c) Rotation velocity V_R of intrinsic polarities during the particle-particle contact, averaged over all particles and time $\langle\cdot\rangle$ vs ω^{CT}. Different marks corresponding to different runs. The plots are fitted by $\langle V_R\rangle = (1.048 \pm 0.002)\omega^{\mathrm{CT}} + (-0.00016 \pm 0.00011)$. 2,048 runs were simulated in total for each ω^{CT}, and each simulation was carried out up to $t = 256$. (d) Time evolution of polar order R_p (red solid curve), nematic order R_n (green dotted curve) and contact numbers (blue broken curve) for the simulation sample identical to (b).

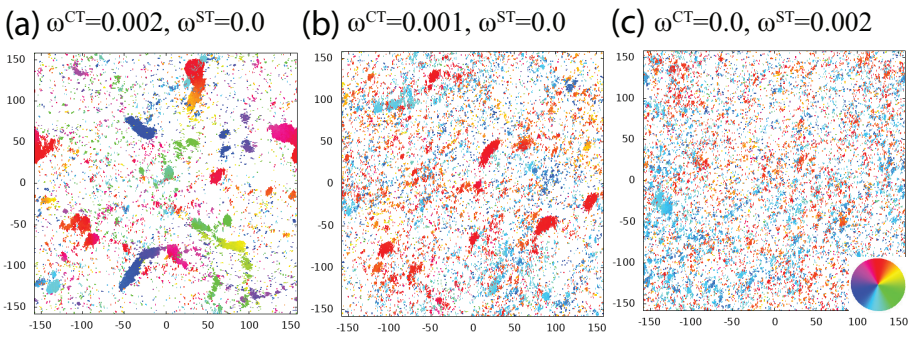

FIG. S3. Dynamic patterns for the case with isotropic friction, $R = 1.0$. Typical snapshots of the numerical results are shown for (a) $\omega^{\mathrm{CT}} = 0.002, \omega^{\mathrm{ST}} = 0.0$, (b) $\omega^{\mathrm{CT}} = 0.001, \omega^{\mathrm{ST}} = 0.0$, and (c) $\omega^{\mathrm{CT}} = 0.0, \omega^{\mathrm{ST}} = 0.002$. $\rho = 0.2$, $\alpha_{\mathrm{AL}} = 1.0$, and $N = 20,000$. Except that the friction is isotropic, these settings are corresponding to those in Fig. 2 of the main text. The mono-polar flocking and bidirectional orientation for the cases with only the CT and only the ST, respectively, are reproduced while typical morphology of each mono-polar flock seems different from that seen in the anisotropic-friction case, where the flock seems to be more elongated (Fig. 2 of the main text).